Impact of ENSO on MJO Pattern Evolution over the Maritime Continent

Jia LIU[1], Yuqin DA[1], Tim LI[1,2*], and Feng HU[1]

1 *Key Laboratory of Meteorological Disaster, Ministry of Education (KLME)/Joint International Research Laboratory of Climate and Environmental Change (ILCEC)/Collaborative Innovation Center on Forecast and Evaluation of Meteorological Disasters (CIC-FEMD), Nanjing University of Information Science & Technology, Nanjing* 210044, *China*

2 *International Pacific Research Center and Department of Atmospheric Sciences, School of Ocean and Earth Science and Technology, University of Hawaii, Honolulu, HI* 96822, *USA*

(Received April 1, 2020; in final form September 10, 2020)

ABSTRACT

The modulation of Madden–Julian oscillation (MJO) pattern evolution over the Maritime Continent (MC) by El Niño–Southern Oscillation (ENSO) was investigated through a combined observational and modeling study. MJO convective branches shifted south of the equator over the MC during eastern Pacific (EP) El Niño winters, while it became relatively symmetric about the equator during La Niña winters. The impact of central Pacific (CP) El Niños to MJO pattern, on the other hand, is not statistically significant. The cause of the distinctive MJO pattern evolutions is likely attributed to the ENSO-induced changes of the background moisture and vertical shear over the MC. Idealized numerical experiments with a 2.5-layer model were carried out, and the result revealed that the background moisture change played a dominant role. An observational diagnosis of column-integrated moist static energy (MSE) budgets was further conducted. The result indicated that the MJO pattern difference was attributed to the MSE tendency asymmetry in front of MJO convection between EP El Niño and La Niña, caused by the advection of the mean MSE by anomalous meridional wind. The difference in the MJO-scale anomalous meridional wind was ultimately controlled by the change of the background meridional moisture gradient associated with EP El Niño and La Niña.

Key words: Madden–Julian oscillation (MJO), El Niño–Southern Oscillation (ENSO), Maritime Continent (MC), moist static energy (MSE) budget

Citation: Liu, J., Y. Q. Da, T. Li, et al., 2020: Impact of ENSO on MJO pattern evolution over the Maritime Continent. *J. Meteor. Res.*, **34**(6), 1151–1166, doi: 10.1007/s13351-020-0046-2.

1. Introduction

The Maritime Continent (MC), commonly used to describe the region between the tropical Indian and Pacific Oceans (10°S–20°N, 90°–150°E), is a key region affecting the earth's climate system. It is made up of thousands of intricate islands, terrains, and shallow seas. The complex land–sea distribution and unique geographic location of the MC are responsible for the rich spectrum of multiscale rainfall variability there, ranging from diurnal cycles to interannual and interdecadal timescales (Zhu et al., 2010; Lu et al., 2019). Extreme weather and climate events often happen over the MC. As it is located in the middle of the warmest body of water in the world (the western Pacific warm pool) with the annual mean sea surface temperature (SST) exceeding 28°C, the MC is dominated by annual mean large-scale ascending motion that transports moisture and heat into the upper troposphere (Ramage, 1968; Li and Hsu, 2018). Serving as the ascending branch of the Walker circulation, the background mean upward motion over the MC is modulated by the interannual variability such as the El Niño–Southern Oscillation (ENSO) and Indian Ocean dipole (IOD; Li et al., 2003). These changes can further affect higher frequency modes such as the Madden–Julian oscillation (MJO), synoptic-scale variability, and diurnal cycle over the MC (Lin and Li, 2008; Rong et al., 2011; Deng and Li, 2016; Deng et al., 2016; Wang et al., 2018).

MJO and ENSO are strongest signals respectively on intraseasonal and interannual timescales (Li and Wang,

Supported by the National Natural Science Foundation of China (42088101 and 41875069), US National Science Foundation (AGS-2006553), and US NOAA Grant (NA18OAR4310298). This is SOEST contribution number 11206 and IPRC contribution number 1494.

*Corresponding author: timli@hawaii.edu.

2005; Li, 2010). Both modes have pronounced influence on global weather and climate (Li et al., 2020; Zhang et al., 2020). First discovered by Madden and Julian (1971, 1972), MJO is characterized by a planetary zonal scale and a slow eastward phase speed along the equator with a characteristic period of 10–90 days (Krishnamurti and Subrahmanyam, 1982; Murakami and Nakazawa, 1985). ENSO, on the other hand, has a spatial scale of thousands of kilometers and a characteristic period of 2–7 yr. After initiated over the western Indian Ocean (Zhao et al., 2013), eastward-propagating MJO often crosses the MC in boreal winter. At the same season, ENSO reaches its peak. The SST anomaly associated with the ENSO induces an anomalous Walker circulation, with anomalous vertical motion right over the MC. It has been shown that such a background vertical motion change associated with El Niño and La Niña can affect MJO strength (Wang et al., 2018). In addition to the contrast between El Niño and La Niña, different types of El Niños [i.e., central Pacific (CP) and eastern Pacific (EP) El Niños; Ashok et al., 2007; Kao and Yu, 2009; Yeh et al., 2009] may also affect the MJO intensity differently (Yuan et al., 2015; Chen et al., 2016). Thus it is important to reveal the fundamental difference of MJO behaviors under different types of ENSO and physical mechanisms behind the observed phenomenon.

While many previous studies showed the large-scale control of ENSO on MJO intensity, it is not clear how the different types of ENSO modulate the MJO pattern evolution over the MC. Mechanisms through which different types of ENSO influence the MJO pattern over the MC are not well resolved. From the moisture mode theory point of view (Raymond, 2000, 2001; Sobel et al., 2001; Maloney, 2009; Sobel and Maloney, 2012, 2013), MJO propagation is primarily determined by the zonal asymmetry of column-integrated moist static energy (MSE) tendency. Through a diagnosis of 27 global general circulation model simulations, Wang et al. (2017) demonstrated that the difference between a good and a poor model group in terms of the MJO simulation capability lies in whether or not these models capture the observed east–west asymmetry of the MSE tendency. A positive MSE tendency in the front of the MJO convection arises from both the horizontal and vertical MSE advections. Thus, by using the MSE diagnostic method, one may reveal the specific processes through which ENSO-induced background states modulate the MJO-scale MSE tendency and thus the MJO pattern.

Motivated by the rationale above, we intend to examine in this study the distinctive MJO pattern evolution characteristics associated with the different types of ENSO and physical mechanisms behind the observed phenomenon based on the MSE budget diagnosis framework. The remaining part of this paper is organized as follows. In Section 2, data and methods are described. In Section 3, observed MJO structure evolution features over the MC during the different types of ENSO events are examined. In Section 4, the background mean states associated with the different ENSO modes are compared, and a simple atmospheric model is used to reveal the relative roles of the background dynamic and thermodynamic fields in regulating MJO activities over the MC. In Section 5, an MSE budget diagnosis is carried out to reveal the mechanism responsible for the MJO structure asymmetry between EP El Niño and La Niña. Finally, conclusions are given in Section 6.

2. Data and methods

The primary datasets used in the current study include Extended Reconstructed Sea Surface Temperature (ERSST; version 3b, monthly, at a grid of 2° longitude by 2° latitude for 1982–2012) from NOAA. The dataset is used to define ENSO years. Intraseasonal signals are extracted from satellite-observed outgoing long-wave radiation (OLR; daily, at a grid of 2.5° longitude by 2.5° latitude for 1979–2013) from NOAA. Interannual background fields are analyzed with ECMWF reanalysis data (ERA-Interim; 4 times daily for 1982–2011). The ERA reanalysis dataset includes the following three-dimensional variables: zonal and meridional wind (u and v), pressure vertical velocity (ω), and specific humidity (q) at 27 pressure levels from 1000 to 100 hPa. The analysis period is focused on boreal winter season [December to February (DJF)] for the period of 1982–2011.

Three types of ENSO events are defined based on the ERSST dataset (Table 1). Among them, EP El Niño is defined when DJF mean SST anomaly averaged over the Niño 3.4 region exceeds one standard deviation (STD). La Niña is defined when DJF mean SST anomaly averaged over the Niño 3.4 region exceeds negative one STD. CP El Niño events are defined based on the temporal-zonal pattern of the SST anomaly (initiated and developed over western-CP and matured in boreal winter), following Chung and Li (2013) and Xiang et al. (2013). For the analysis period only four CP El Niño events (1994, 2002, 2004, and 2009) are identified.

Applying a 10–90-day Lanczos band-pass filter onto the daily observed OLR field, one may extract intraseasonal OLR signals. At each winter, the STD of 10–90-day filtered OLR anomaly is used to measure the intensity of the MJO. By composing the MJO intensity in

different types of ENSO events, one may further examine the dependence of MJO strength on ENSO type at each grid point. The MJO pattern evolution characteristics are then derived from the lead–lag time regression against the time series of the 10–90-day band-pass-filtered OLR anomaly at a reference point (5°S, 95°E), where MJO is most active in boreal winter. The climatology annual cycle of the OLR field is removed before the band-pass filtering.

A composite analysis on horizontal wind, vertical p-velocity, specific humidity, and vertical shear fields is utilized to reveal the difference of the interannual background states during the different types of ENSO. A Student's t test is applied to examine whether the difference is statistically significant.

A 2.5-layer theoretical model developed by Wang and Li (1993, 1994) is applied to understand the relative importance of the background dynamic and thermodynamic fields in influencing MJO behavior over the MC. The 2.5-layer model was previously used for the study of MJO dynamics (Li and Wang, 1994; Wang and Li, 1994; Wang and Xie, 1997; Jiang et al., 2004; Li and Zhou, 2009). This model consists of a 2-layer free atmosphere and a well-mixed planetary boundary layer (PBL) at a horizontal domain of 40°S–40°N, 0°–360°. A three-dimensional background mean state is specified in this anomaly model so that one may focus on examining the evolution of an MJO-like perturbation under different background mean states.

To reveal the cause of distinctive MJO propagation behaviors under El Niño and La Niña conditions, a column-integrated MSE budget analysis is conducted. MSE (m) may be defined as $m = c_pT + gz + L_vq$, where T denotes temperature, z height, q specific humidity, $c_p = 1004\ \mathrm{J\ K^{-1}\ kg^{-1}}$ is the specific heat at constant pressure, $g = 9.8\ \mathrm{m\ s^{-2}}$ is the gravitational acceleration, and $L_v = 2.5 \times 10^6\ \mathrm{J\ kg^{-1}}$ is the latent heat of vaporization.

According to Neelin and Held (1987), column-integrated MSE budget can be written as:

$$\langle \partial_t m \rangle = -\omega \left\langle \partial_p m \right\rangle - \langle \boldsymbol{V} \cdot \nabla m \rangle + Q_t + Q_r, \qquad (1)$$

where ω denotes vertical pressure velocity, p pressure and $\boldsymbol{V}$ horizontal wind vector, and angle brackets a mass-weighted vertical integral from 1000 to 200 hPa. The left-hand side (lhs) of the equation above represents the MSE tendency and the right-hand side (rhs) terms represent, from left to right, vertical advection, horizontal advection, surface heat flux, and vertically integrated radiative heating rate; Q_t and Q_r are calculated based on ERA-Interim.

3. MJO evolution characteristics over the MC during different types of ENSO

As stated in Section 2, the STD of 10–90-day filtered OLR anomaly is used to measure the MJO intensity at each year. Figure 1 shows the 10–90-day filtered OLR STD anomalies averaged during EP El Niño years, CP El Niño years, and La Niña years. A marked large-scale negative STD anomaly appears in EP El Niño composite over the northern MC (green box in Fig. 1), where a positive STD anomaly appears in the La Niña composite. The STD anomaly appears much weaker and not statistically significant in the CP El Niño composite. The result indicates that EP El Niño and La Niña exert a significant impact on MJO behavior over the MC, in particular northern MC, whereas the CP El Niño's influence on MJO is weak and statistically insignificant. Therefore, we will focus on examining the modulation of MJO pattern and evolution characteristics over the MC by EP El Niño and La Niña.

Figure 2 illustrates distinctive MJO pattern evolution characteristics during EP El Niño and La Niña winters. It is noted that after reaching the eastern Indian Ocean, the main MJO convective branches shift southward during EP El Niño (left panel of Fig. 2). Such a southward shifting over the MC is not clearly seen in the La Niña composite. The MJO convective branches are approximately symmetric about the equator (right panel of Fig. 2).

The distinctive pattern evolution features shown in Fig. 2 reflect well the MJO variability difference over the northern MC (i.e., the green box in Fig. 1). Over the region, the MJO variability is enhanced during La Niña but significantly suppressed during EP El Niño. The overall intensity of the MJO over the equatorial MC is stronger during La Niña composite than during EP El Niño composite, as seen from the longitude–time maps of the OLR and MSE anomalies averaged on the equator (Fig. 3).

The distinctive MJO pattern evolution behaviors are likely attributed to the impact of the background mean state changes associated with EP El Niño and La Niña. Figure 4 illustrates low-level wind and specific humidity anomaly fields in EP El Niño and La Niña composites. Note that there is a strong anticyclone anomaly over the green box region during EP El Niño winters, while a cyclone anomaly appears in La Niña winters. The anomal-

Table 1. List of EP and CP El Niño years and La Niña years

ENSO type	Year
EP El Niño	1982, 1986, 1991, 1997
La Niña	1984, 1988, 1999, 2007, 2010
CP El Niño	1994, 2002, 2004, 2009

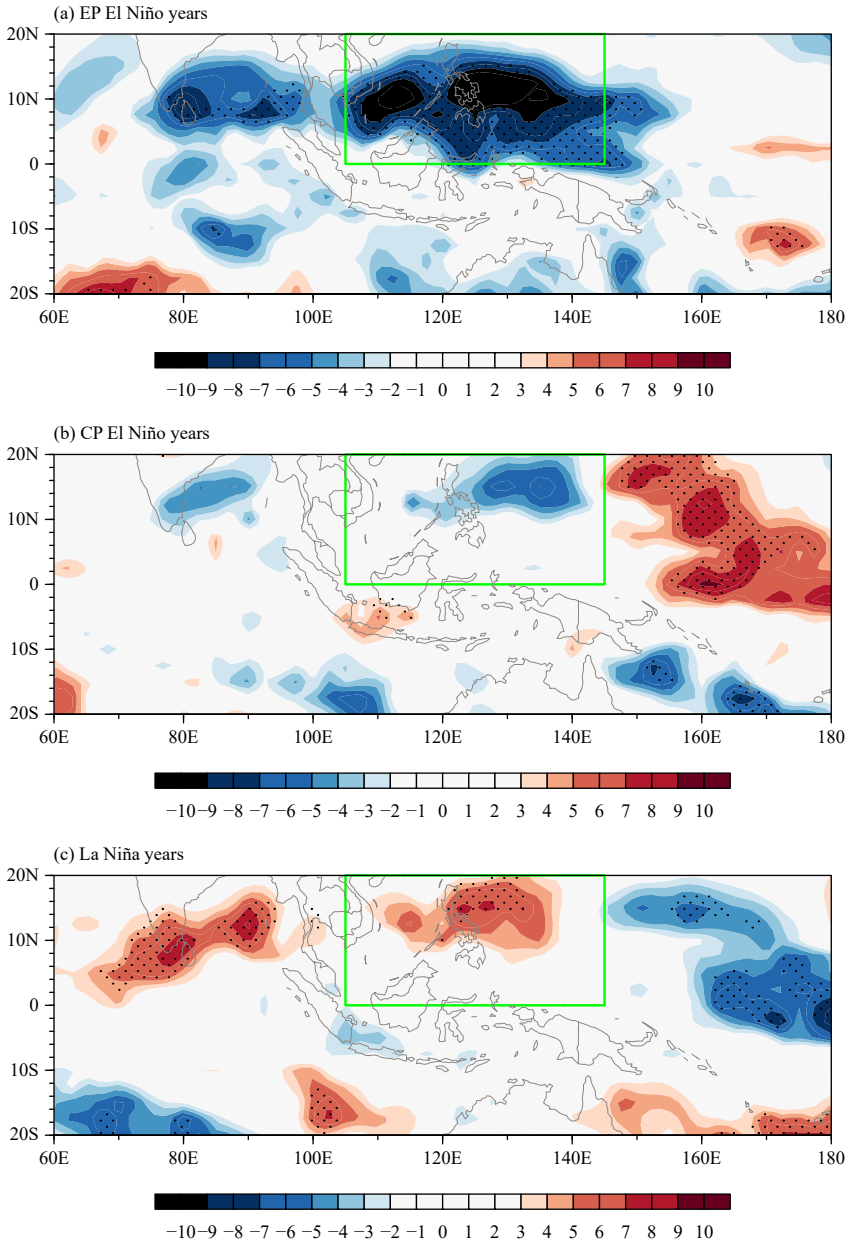

Fig. 1. Standard deviation (STD) of 10–90-day band-pass filtered OLR anomalies (shaded; W m^{-2}) for (a) EP El Niño, (b) CP El Niño, and (c) La Niña. Climatological STD at each grid point has been subtracted at each panel. The green box denotes a key region (0°–20°N, 105°–145°E) where ENSO exerts a strong impact on MJO.

ous anticyclone during El Niño was referred to as the Philippine Sea anticyclone (PSAC; Wang et al., 2003) or the western North Pacific anticyclone (WNPAC; Wu et al., 2009, 2010; Li et al., 2017). The low-level anticyclone (cyclone) anomaly may further induce anomalous PBL divergence (convergence) and thus anomalous descending (ascending) motion in situ through the Ekman pumping effect. The anomalous descending (ascending) motion decreases (increases) local moisture through vertical advection. As a result, a negative specific humidity anomaly occurs in northern MC during EP El Niño, whereas a positive specific humidity anomaly occurs during La Niña.

The vertical distributions of box-averaged zonal wind, vorticity, specific humidity, and vertical velocity fields (Fig. 5) do present significant differences between the EP El Niño and La Niña background states. Negative specific humidity and vorticity anomalies and anomalous descent occur throughout the troposphere over the northern MC during EP El Niño winters (Figs. 5b–d). In contrast, positive specific humidity and vorticity anomalies and anomalous ascent appear during La Niña winters.

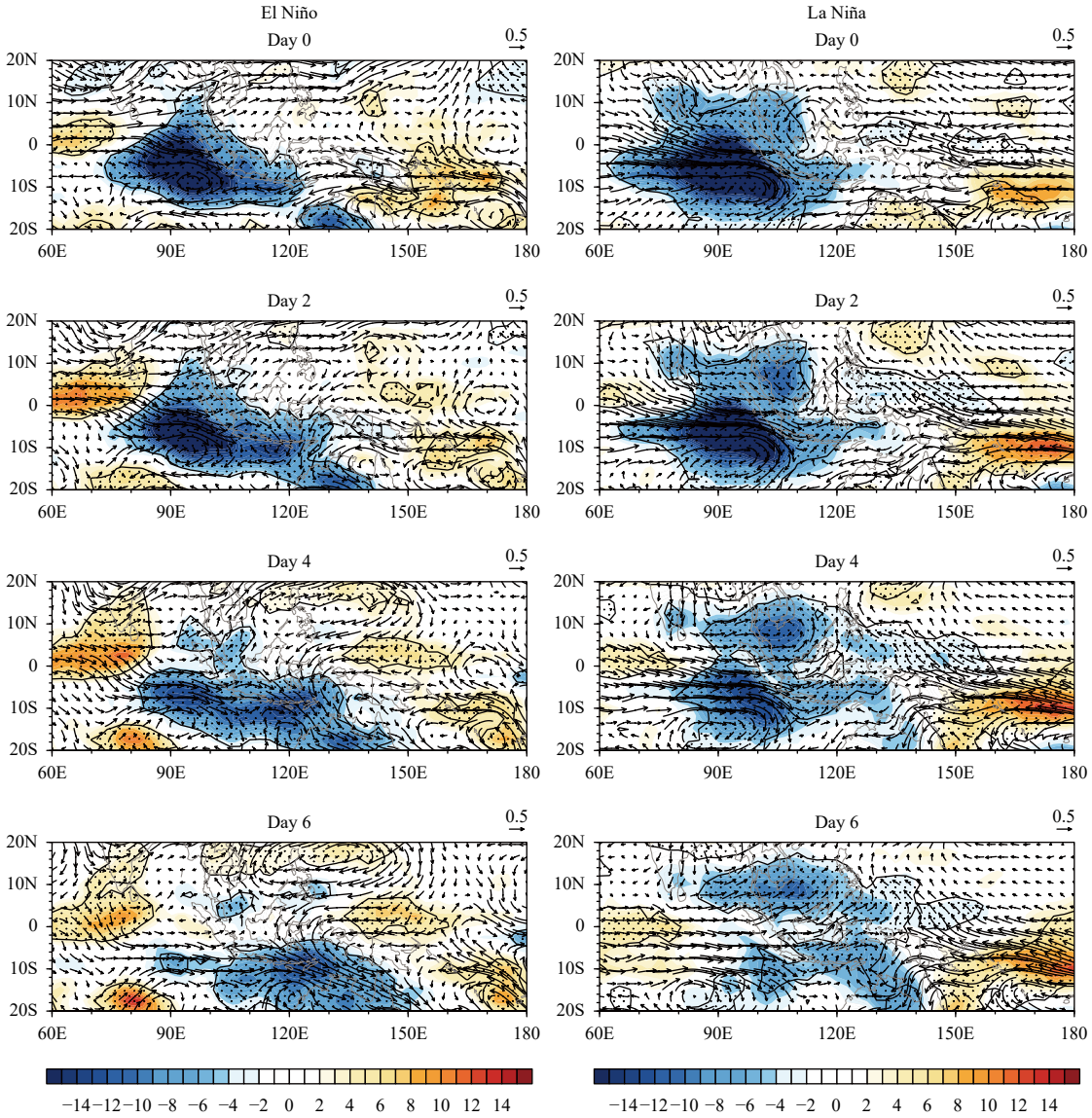

Fig. 2. Lead–lag regressed patterns of 10–90-day filtered OLR anomaly (shaded; W m^{-2}) and associated wind anomaly field at 850 hPa (vector; m s^{-1}) from Days 0 to 6. The regression was based on the OLR anomaly at a reference point over Indian Ocean (5°S, 95°E) for EP El Niño (left) and La Niña (right) winters. The OLR anomalies that pass the significant test at 95% confidence level are stippled.

An interesting feature is the contrast of vertical profiles of zonal wind between EP El Niño and La Niña. A westerly (easterly) vertical shear anomaly appears during EP El Niño (La Niña) (Fig. 5a). Previous studies demonstrated that the easterly shear could strengthen tropical disturbances through barotropic–baroclinic mode coupling (Wang and Xie, 1996). Due to the coupling, lower-tropospheric perturbation is strengthened, which may promote a greater mid-tropospheric heating through Ekman pumping induced moisture convergence (Li, 2006; Ge et al., 2007).

The observational analysis results above suggest that the change of the background dynamic and thermodynamic states associated with ENSO may modulate the MJO intensity and propagation over the MC. However, the relative role of the dynamic and thermodynamic states is not clear. This scientific question will be addressed in the next section with the use of a simple atmospheric model.

4. Relative roles of ENSO background dynamic and thermodynamic states in regulating MJO activities over MC

A 2.5-layer atmospheric model is used to examine the relative role of the background dynamic and thermodynamic states associated with ENSO in modulating MJO activities. Three sets of idealized numerical model exper-

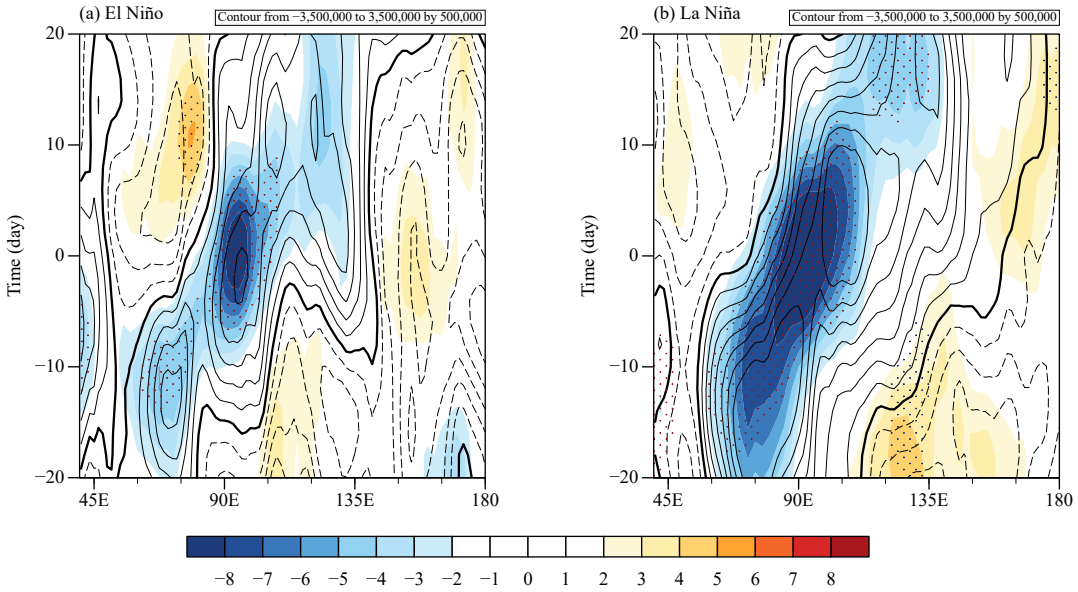

Fig. 3. The Hovmöller diagram of the regressed OLR (shaded; W m^{-2}) and column-integrated MSE (contour; J m^{-2}) anomalies averaged over 20°S–20°N for (a) EP El Niño and (b) La Niña winters from Days −20 to 20. The regression was based on the OLR anomaly at 5°S, 95°E. The OLR anomalies that pass the significant test at 95% confidence level are stippled.

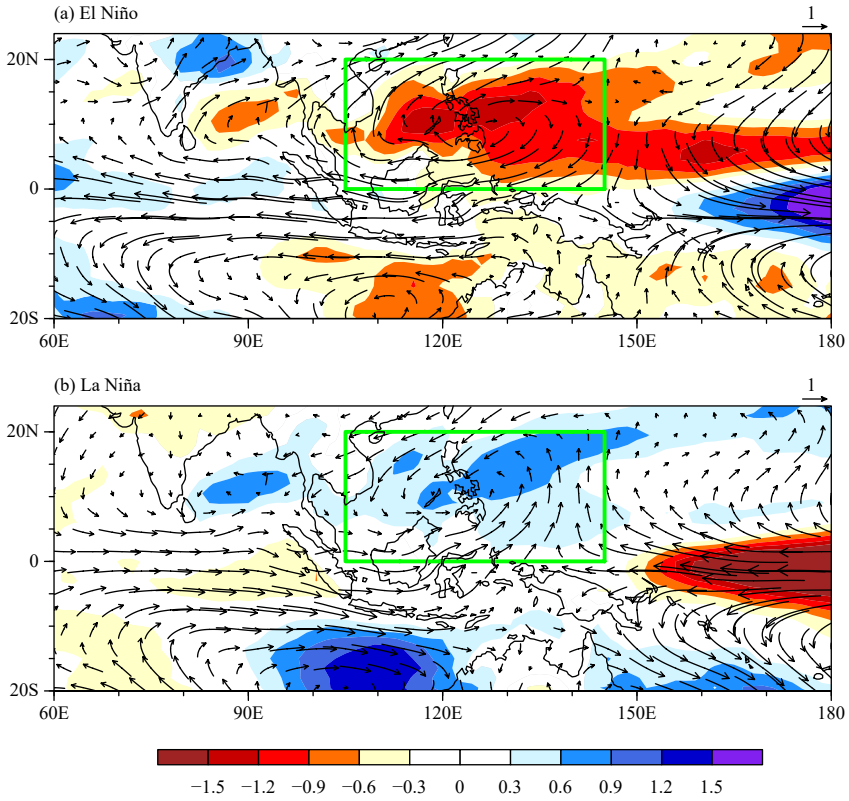

Fig. 4. Background specific humidity (shaded; g kg^{-1}) and 850-hPa wind (vector; m s^{-1}) fields during (a) El Niño and (b) La Niña winters (DJF). Climatological mean specific humidity and 850-hPa wind fields have been subtracted at each panel. The green box shows the same region as that in Fig. 1.

iments were carried out (see Table 2). First, a control experiment (CTL) is conducted to verify the model's ability of simulating the MJO-like perturbation in the tropics. In this experiment, the observed boreal winter mean state

from ERA reanalysis is specified. Next, two sensitivity experiments were designed. In EXP1, a horizontal uniform specific humidity anomaly field derived from area-averaged values in northern MC (Fig. 5d) is superposed onto the observed winter mean background state to mimic the ENSO thermodynamic impact. In EXP2, a uniform vertical shear anomaly field is superposed onto the observed winter mean background state to mimic the ENSO dynamic impact. Specifically, a constant value of 0.8 g kg^{-1} (which is equal to a half of the area-averaged specific humidity difference at 750 hPa between La Niña and El Niño composite) is added to the seasonal mean moisture field in EXP1. A constant value of vertical wind shear (u_{200} minus u_{850}) of −6.5 m s^{-1} is added to the seasonal mean zonal wind field in EXP2.

Table 2. Description of the control and sensitivity numerical experiments

Name of experiment	Background mean state
CTL	Observed u, v, t, q, SST, ω, and Φ in DJF
EXP1	CTL + a uniform specific humidity anomaly
EXP2	CTL + a uniform vertical wind shear anomaly

The evolution of simulated low-level wind and precipitation anomalies in the CTL run is shown in Fig. 6. An MJO-like perturbation moves slowly eastward along the equator. The main convective branch crosses the MC during Days 4–7. The horizontal pattern of the MJO shows a Kelvin–Rossby wave couplet structure (Li and Wang, 1994; Wang and Li, 1994), consistent with the observed (Hendon and Salby, 1994).

The relative roles of the background moisture and vertical wind shear change in regulating MJO intensity may be revealed through the analysis of the two sensitivity experiments EXP1 and EXP2. Figure 7 shows the amounts of accumulated (Days 4–7) precipitation anomalies over the MC region derived from CTL, EXP1, and EXP2. It indicates that the ENSO-induced background moisture difference plays a dominant role in modulating the MJO intensity, whereas the vertical shear difference appears

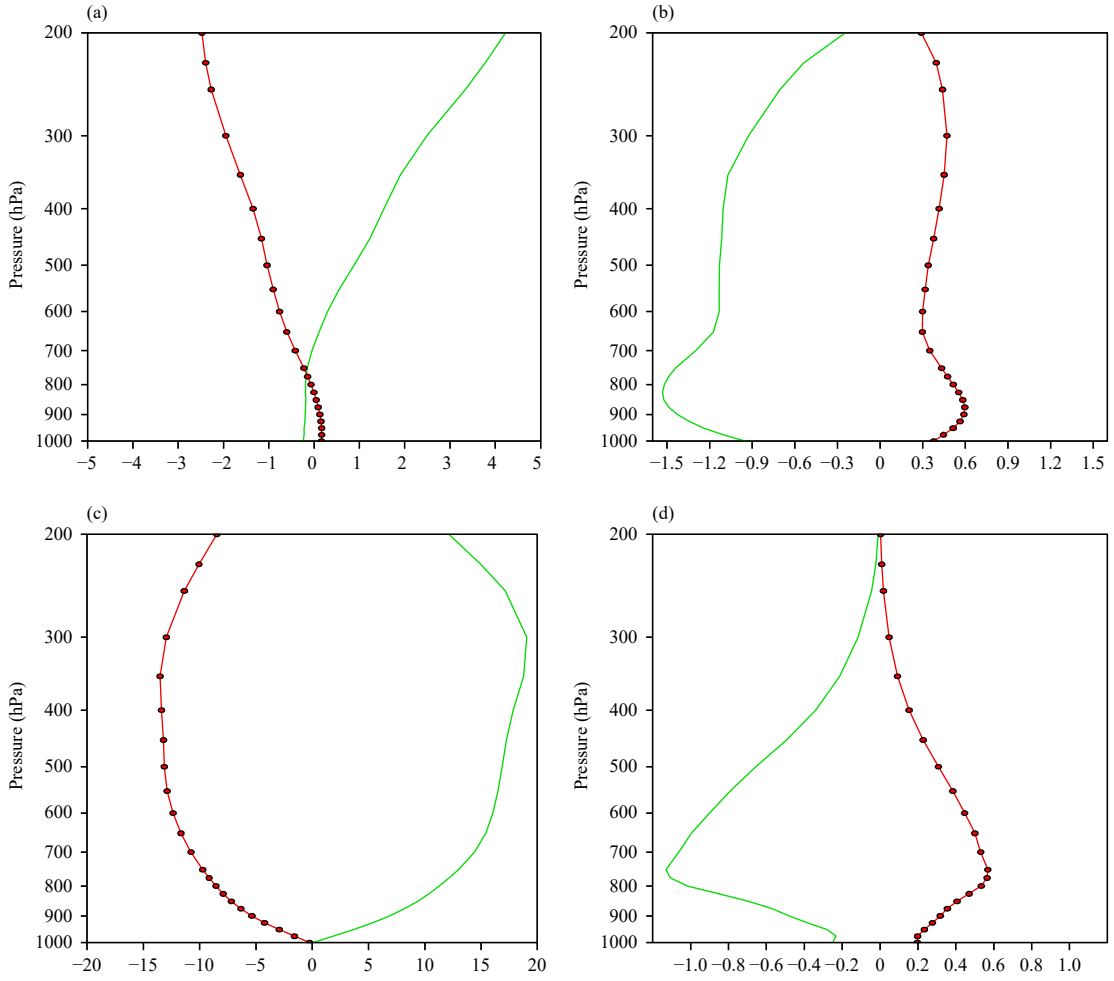

Fig. 5. Vertical profiles of (a) background zonal wind (m s^{-1}), (b) vorticity (10^{-6} s^{-1}), (c) vertical p-velocity (10^{-3} Pa s^{-1}), and (d) specific humidity (g kg^{-1}) averaged over the green box (0°–20°N, 105°–145°E) shown in Fig. 1 for EP El Niño (green) and La Niña (red) years.

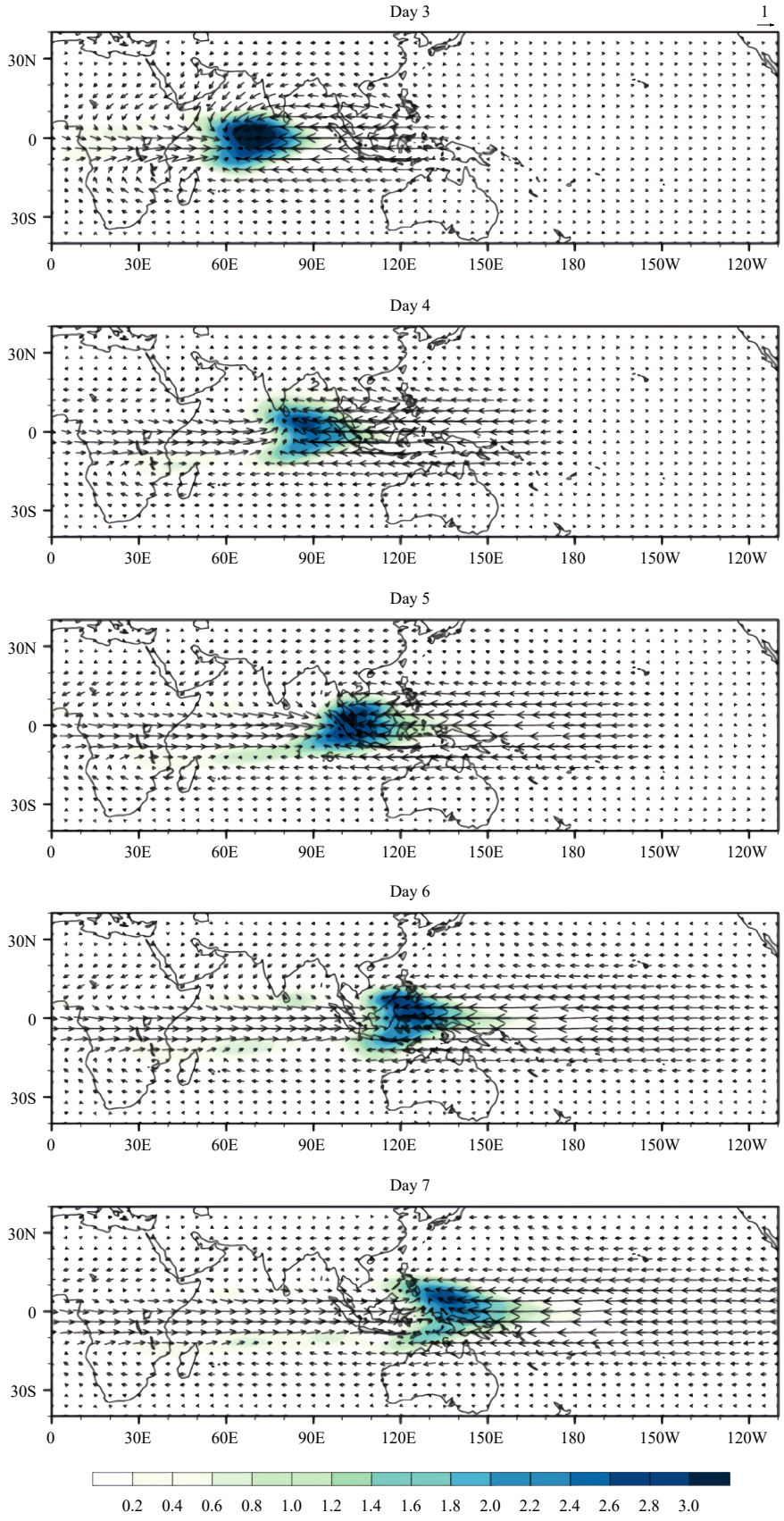

Fig. 6. Time evolutions of lower-tropospheric wind (vector; m s^{-1}) and precipitation (shaded; mm day^{-1}) anomaly fields of an MJO-like perturbation from Days 3 to 7, simulated by a simple atmospheric model.

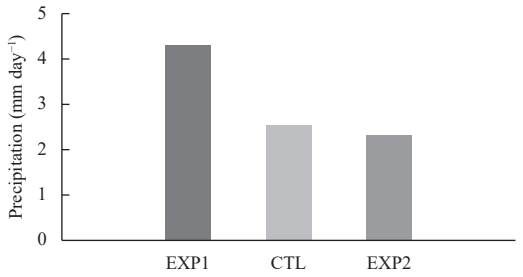

Fig. 7. Accumulated (Days 4–7) precipitation anomalies as the MJO-like disturbance passes over the MC in CTL, EXP1, and EXP2.

unimportant. Therefore, the numerical model experiments suggest that the ENSO modulation on the MJO is primarily through the change of the background moisture field.

5. Cause of the MJO pattern evolution asymmetry between EP El Niño and La Niña—An MSE budget diagnosis

An important feature of the MJO pattern evolution over the MC during EP El Niño is the southward shift of the MJO main convective branches. This is in contrast to an approximately equatorially symmetric pattern during La Niña. The cause of this pattern asymmetry is to be addressed through a column-integrated MSE budget analysis. It was noted that the MJO convective center was approximately in phase with the anomalous MSE center (Jiang et al., 2015; Wang et al., 2017). For the eastward-moving MJO, a positive MSE tendency was located in front of the MJO convective center. Thus, in the subsequent analysis, we will focus on the MSE budget diagnosis in front of the MJO convective center.

Figure 8 shows the horizontal patterns of the anomalous MSE tendency fields (contour) when the MJO main convection is located over the eastern Indian Ocean (around 95°E). There is a clear equatorial asymmetry in the MSE tendency field east of the MJO convective center during El Niño (top panel of Fig. 8). A negative (positive) tendency appears north (south) of the equator, as shown in the red (blue) box. In contrast, during La Niña the MSE tendency field is approximately symmetric. This implies that during El Niño the MJO convection is strengthened (weakened) south (north) of the equator over the MC, whereas during La Niña, the MJO convection is strengthened at both sides of the equator.

The MSE tendency patterns shown in Fig. 8 reflect well the MJO pattern evolution characteristics shown in

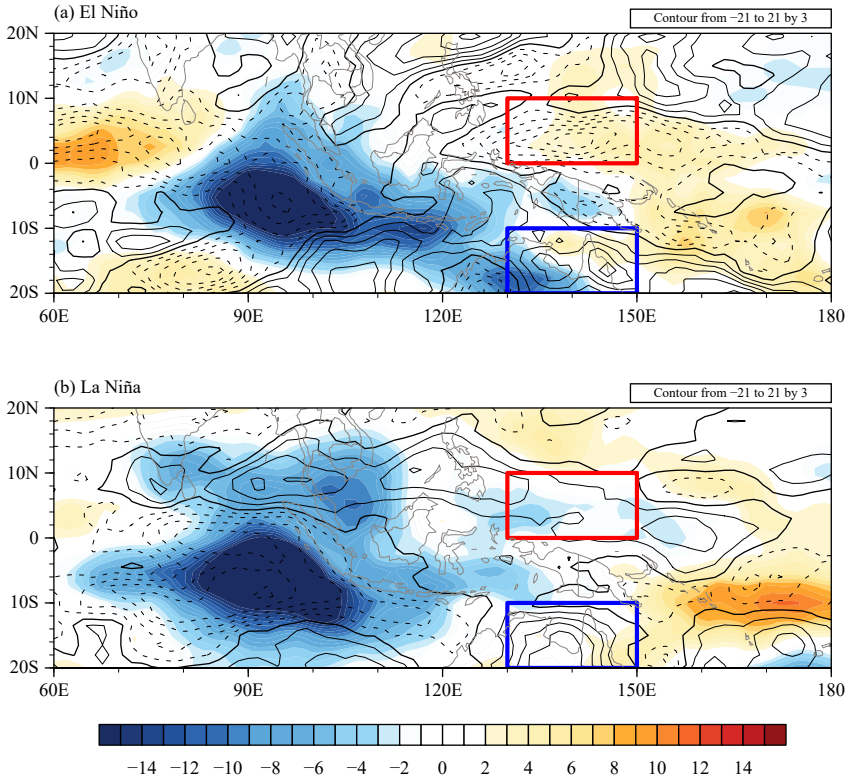

Fig. 8. Horizontal patterns of the OLR anomaly (shaded; W m^{-2}) and column-integrated MSE tendency (contour; W m^{-2}) fields regressed onto the OLR anomaly at the reference point (5°S, 95°E) for EP El Niño (top) and La Niña (bottom) winters. The red and blue boxes are key regions for the MSE budget analysis in front of the MJO convection.

Fig. 2. Note that there is a slight asymmetry about the equator between the blue and red boxes. This is because the maximum MJO convective center in boreal winter shifts slightly southward over the Indian Ocean, as seen from the OLR anomaly centers in Fig. 8. Thus, the MSE tendency pattern difference over the northern and southern boxes can be used to understand the overall MJO structure asymmetry between EP El Niño and La Niña.

What causes the MSE tendency difference in front of MJO convection between El Niño and La Niña? To address this question, we conduct an MSE budget diagnosis over the two key regions (i.e., the red and blue boxes in Fig. 8). The box-averaged MSE budget results are shown in Fig. 9. Over the southern box (box2), the MSE tendencies are almost the same for both EP El Niño and La Niña, and the main difference appears in the northern box (box1). Thus, we will pay special attention to the MSE budgets over the northern box.

Figure 10 shows each of the MSE budget terms averaged over the northern (red) and southern (blue) boxes. A clear north–south asymmetry in the MSE tendency appears during EP El Niño but not during La Niña. The difference map between La Niña and El Niño (Fig. 10c) shows that the main difference lies in the meridional advection term. This term has an opposite sign between the northern and southern boxes. By decomposing each variable into three components [i.e., climatological annual cycle, interannual component (2–7 yr), and high frequency components (< 90 days)], one may have

$$v = v_1 + v_2 + v_3, \tag{2}$$

and

$$m = m_1 + m_2 + m_3. \tag{3}$$

Thus, the meridional advection term may be separated into nine terms.

Figure 11 shows the total and decomposed meridional advection terms over the northern box during EP El Niño and La Niña and their difference. It is clearly seen from the difference map (Fig. 11c) that the dominant term that causes the MSE tendency difference between EP El Niño and La Niña lies on the advection of the climatological mean MSE by the intraseasonal wind anomaly ($-v_3\partial m_1/\partial y$).

To investigate the cause of the distinctive difference of the meridional advection term between EP El Niño and La Niña, we plotted their vertical distributions. As seen in Fig. 12, the vertical profiles have a maximum in middle and lower troposphere (around 800–600 hPa) in both the EP El Niño and La Niña composites. Thus, to understand how the ENSO background states modulate the MSE tendency, we further examine the anomalous circulation and the climatological mean MSE fields averaged over 800–600 hPa.

Figure 13 illustrates the horizontal patterns of the mean MSE and the MJO-scale wind fields averaged over 800–600 hPa. The climatological mean MSE has a maximum center slightly south of equator in boreal winter. Over the northern box (green box in Fig. 13), the mean MSE decreases with increased latitude, and as a result, there is a negative meridional MSE gradient. It is inter-

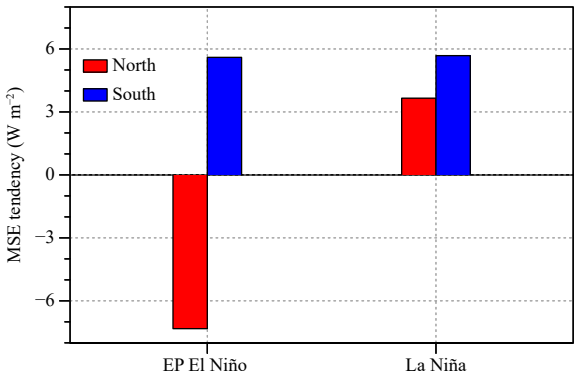

Fig. 9. MSE tendency (W m^{-2}) anomalies averaged over the northern (red) and southern (blue) boxes shown in Fig. 8 for EP El Niño (left) and La Niña (right).

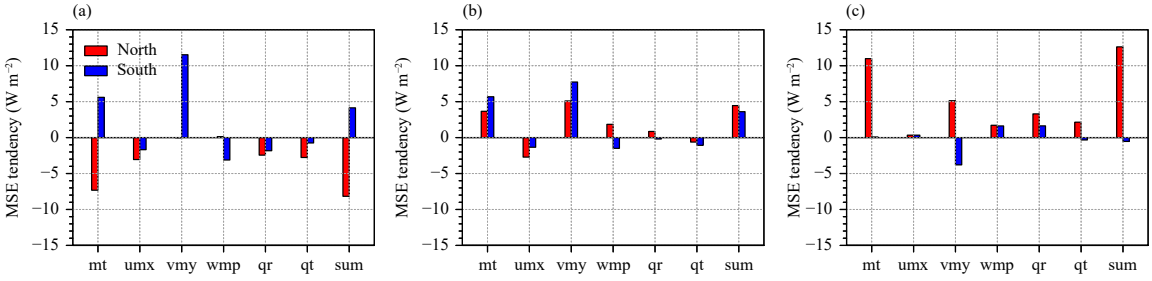

Fig. 10. MSE budget terms (W m^{-2}) averaged over the northern (red) and southern (blue) boxes shown in Fig. 8 for (a) EP El Niño winters, (b) La Niña winters, and (c) their difference (La Niña minus EP El Niño). Bars from left to right represent MSE tendency (mt), zonal advection (umx), meridional advection (vmy), vertical advection (wmp), vertically integrated radiative heating (qr), surface heat flux (qt), and sum of all budget terms on rhs of the MSE budget equation (sum).

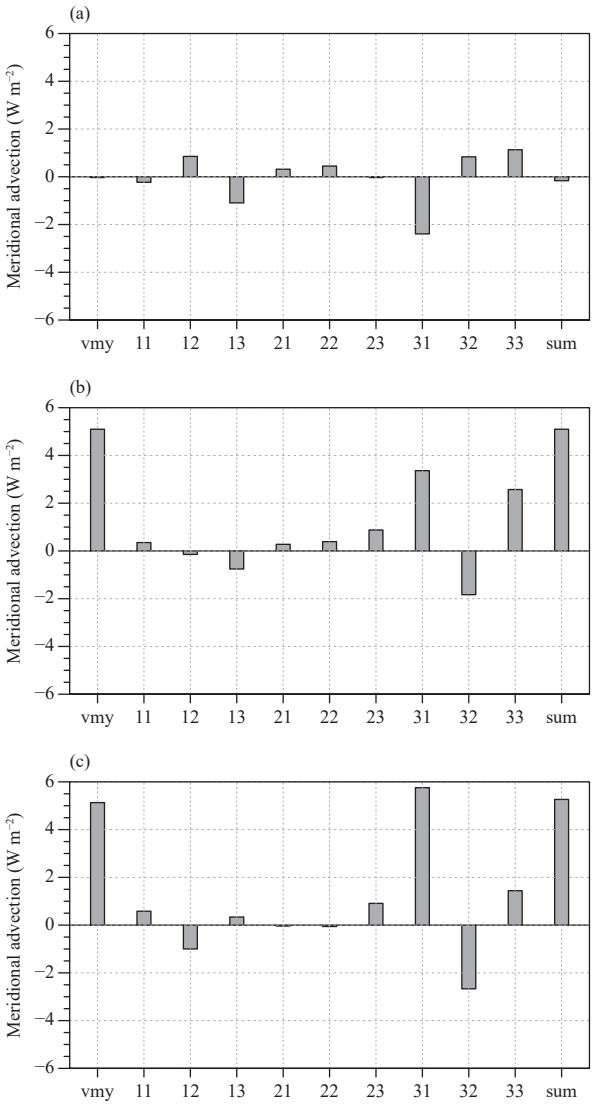

Fig. 11. Decomposition of the anomalous meridional MSE advection term ($-\langle v\partial m/\partial y\rangle'$; W m^{-2}) averaged over the northern box (red box in Fig. 8) for (a) EP El Niño, (b) La Niña, and (c) their difference (La Niña minus EP El Niño). Bars from left to right represent total and each component of the meridional advection term: $-\langle v\partial m/\partial y\rangle'$, $-\langle v_1\partial m_1/\partial y\rangle'$, $-\langle v_1\partial m_2/\partial y\rangle'$, $-\langle v_1\partial m_3/\partial y\rangle'$, $-\langle v_2\partial m_1/\partial y\rangle'$, $-\langle v_2\partial m_2/\partial y\rangle'$, $-\langle v_2\partial m_3/\partial y\rangle'$, $-\langle v_3\partial m_1/\partial y\rangle'$, $-\langle v_3\partial m_2/\partial y\rangle'$, $-\langle v_3\partial m_3/\partial y\rangle'$, and the sum of the nine decomposed terms. Here subscripts 1, 2, and 3 denote the climatological annual cycle, interannual, and high frequency (< 90 days) components.

esting to note that within the box there is anomalous southward (northward) wind during El Niño (La Niña). The southward (northward) wind would generate a negative (positive) meridional MSE advection, contributing to an MSE tendency asymmetry between EP El Niño and La Niña. Therefore, the asymmetric meridional wind in the northern box holds a key for understanding the EP El Niño–La Niña difference.

It is hypothesized that the distinctive MJO-scale meridional wind difference arises from the impact of the

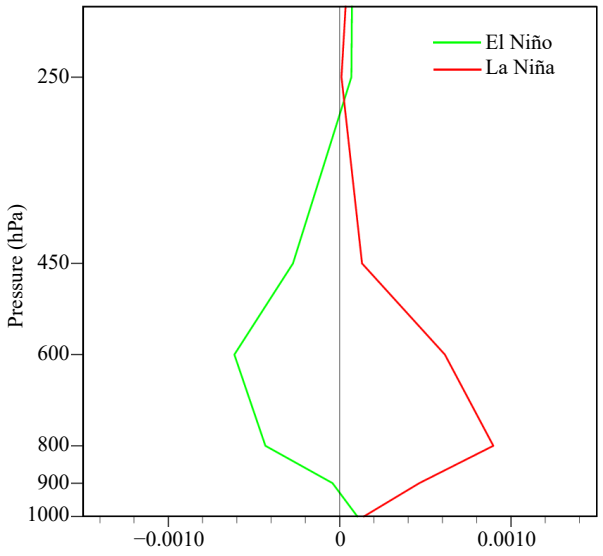

Fig. 12. Vertical profiles of term $-\langle v_3\partial m_1/\partial y\rangle'$ (i.e., advection of the mean MSE by intraseasonal meridional wind; W m^{-2}) averaged over the northern box (red box in Fig. 8) during EP El Niño (green) and La Niña (red) winters.

background mean state. Note that the climatological mean moisture over the MC longitudes in DJF is greater south of the equator than north of the equator. This superposes to the dry (wet) condition north of the equator (Fig. 4), strengthening (reducing) the background north–south moisture gradient during EP El Niño (La Niña). As a result, the MJO convection shifts southward over the MC during EP El Niño, which induces anomalous southward cross-equatorial low-level flow. On the other hand, during La Niña the MJO convection is more symmetric about the equator (Fig. 2b), and the northward wind anomaly north of the equator is a result of a suppressed heating in front of MJO convection caused by Kelvin-wave-induced vertical overturning circulation (Gill, 1980; Wang et al., 2017).

The equatorially asymmetric circulation pattern to the east of MJO convection during EP El Niño may be further deduced from the meridional distribution of lower-tropospheric vertical velocity field (Fig. 14). During EP El Niño, the vertical velocity anomaly to the east of the MJO convection has an opposite sign between northern and southern region. Anomalous ascent (descent) motion associated with the MJO appears to the south (north) of the equator. Such a meridional overturning circulation is associated with anomalous southward flow at low level. In contrast, the vertical velocity field during La Niña is approximately symmetric about the equator. Anomalous upward motion appears in both sides of the equator.

To sum up, the MSE budget analysis indicates that the distinctive MJO pattern asymmetry over the MC between

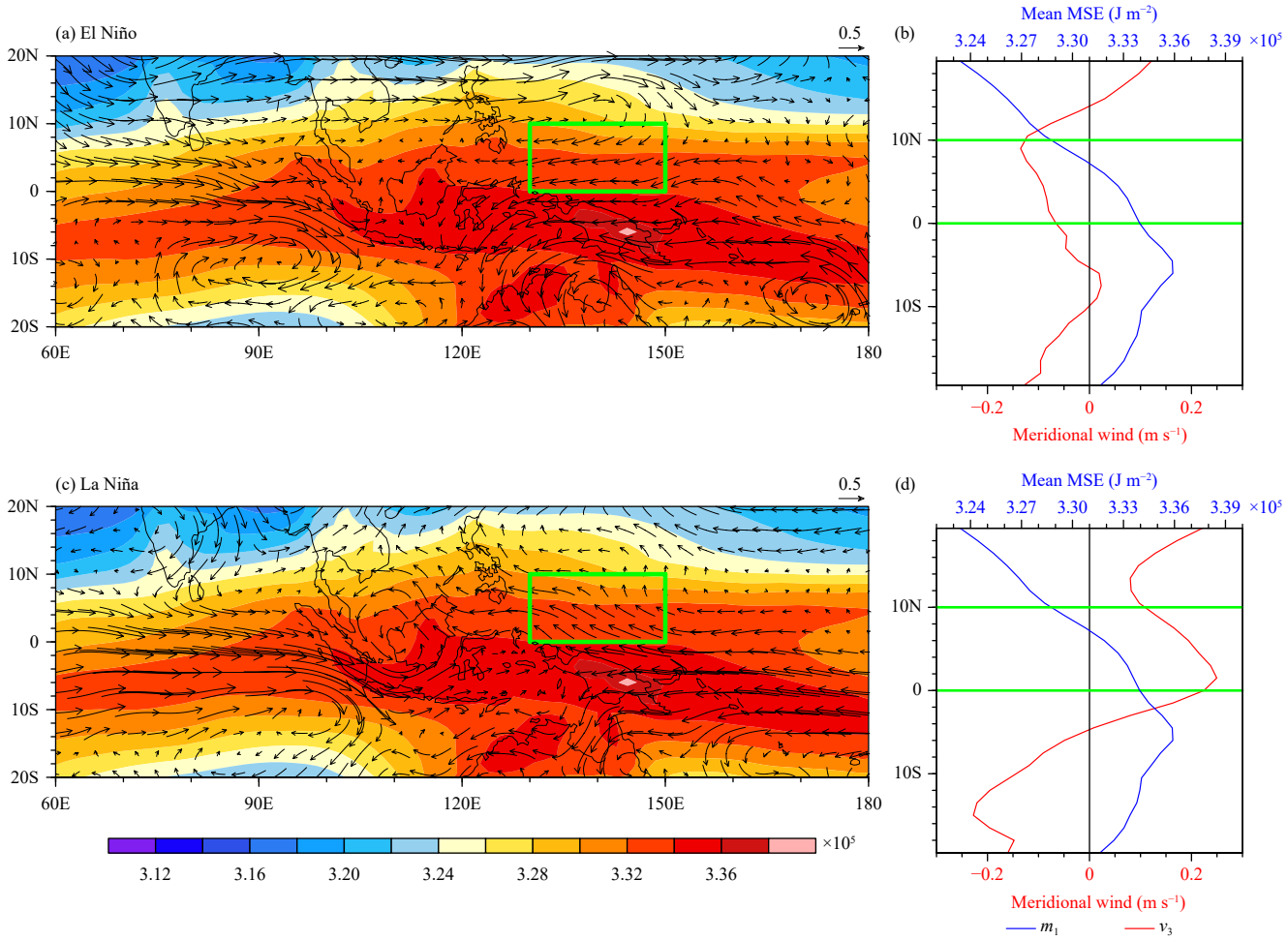

Fig. 13. Horizontal patterns of the climatological mean MSE (shaded; J m^{-2}) and intraseasonal wind (vector; m s^{-1}) fields averaged over 800–600 hPa. Right panels show the meridional distributions of the mean MSE (m_1; blue) and anomalous meridional wind (v_3; red) averaged over 130°–150°E during (a, b) EP El Niño and (c, d) La Niña winters.

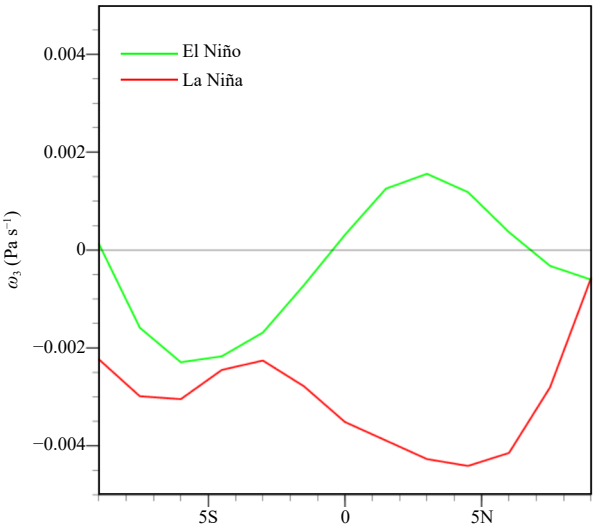

Fig. 14. Meridional distributions of the regressed vertical p-velocity anomaly (ω_3; Pa s^{-1}) at 700 hPa averaged over 130°–150°E for EP El Niño (green) and La Niña (red) winters. The regression was based on the time series of the OLR anomaly at the reference point (5°S, 95°E).

EP El Niño and La Niña results from the distinctive anomalous meridional advections north of the equator. The difference of the MJO-scale meridional wind in front of the MJO convection between EP El Niño and La Niña results from the impact of ENSO-induced change of the background moisture distribution. A more symmetric (asymmetric) background moisture distribution over the MC during La Niña (EP El Niño) leads to a more symmetric (asymmetric) MJO structure relative to the equator. Therefore, the background states associated with the EP El Niño and La Niña play an important role in promoting the distinctive MJO structure characteristics.

6. Conclusions and discussion

In this study, we revealed distinctive MJO pattern evolution characteristics during EP El Niño and La Niña. The MJO convective branch shifted southward over the MC region during EP El Niño winters, whereas it distrib-

uted more symmetrically about the equator during La Niña. The impact of CP El Niño on the MJO structure, on the other hand, is not statistically significant. As a result, the MJO pattern over the MC during CP El Niño resembled the long-term climatology.

As a result of the pattern asymmetry, the most sensitive region of the ENSO impact on the MJO is in northern MC (0°–20°N, 105°–145°E). The MJO convective variability in the region is substantially weakened during EP El Niño but strengthened during La Niña.

The distinctive MJO pattern evolution characteristics are possibly attributed to the background moisture and vertical shear changes associated with EP El Niño and La Niña. A negative specific humidity anomaly and an anomalous anticyclone, accompanied by anomalous descent and westerly vertical shear, occurred over the northern MC during EP El Niño winters. A nearly mirror image pattern of the circulation and moisture anomalies appeared during La Niña winters. Sensitivity experiments with a 2.5-layer model were conducted to understand the relative role of the background moisture and vertical shear changes. The numerical model results suggest that the background moisture field is critical in affecting the MJO strength.

The distinctive MJO pattern evolution characteristics between EP El Niño and La Niña were further examined through an MSE budget analysis. Note that the MSE tendency in front of the MJO convective center reflected well the MJO structure asymmetry over the MC. A negative (positive) MSE tendency appeared over northern MC during EP El Niño (La Niña). The difference arose primarily from anomalous meridional MSE advection. By further decomposing the meridional advection term into nine terms, we found that the main contributor was the advection of the mean MSE by the MJO-scale meridional wind. A southward (northward) wind anomaly appeared over northern MC during EP El Niño (La Niña). Such an MJO-scale circulation asymmetry arose from the distinctive meridional background moisture distributions during EP El Niño and La Niña. Superposed on the climatological mean state, an equatorially asymmetric (symmetric) background moisture distribution occurred during EP El Niño (La Niña). This led to an equatorially asymmetric (symmetric) intraseasonal wind distribution over the MC during EP El Niño (La Niña). Thus the ENSO-modified background meridional moisture gradient played a fundamental role in causing the distinctive MJO pattern evolutions over the MC.

A limitation of the current analysis is that the data used are only up to 2012. A further examination of the data in the recent period (up to 2019) reveals that only 2015 (2017) event satisfies the definition of an EP El Niño (a La Niña) described in Section 2. Figure 15 illustrates the MJO pattern evolutions during the 2015 and 2017 winters. The MJO pattern evolutions resemble in general the composite result shown in Fig. 2, that is, the main convective branch associated with the MJO shifted southward over the MC longitudes during EP El Niño, whereas it appeared more symmetric about the equator during La Niña.

An issue is how to reasonably separate the EP and CP El Niño events. Currently there were various definitions about CP El Niño (see a detailed discussion on this topic in Xiang et al., 2013). Most of the definitions were based on the longitudinal location of anomalous SST centers during El Niño mature winter. However, using these definitions, some mixed events (with SST anomaly centers shifted during their life cycle) might be regarded as a CP El Niño event. We argue that a definition based on the temporal evolution of an El Niño during its entire life cycle is more reasonable, as discussed in Xiang et al. (2013). With the full consideration of the El Niño temporal evolution feature, Xiang et al. (2013) identified four CP El Niño events (1994, 2002, 2004, and 2009) since 1980. Interestingly, the four events are only common cases among all the existing CP El Niño definitions (Xiang et al., 2013).

A caution is needed in interpreting the simple model result, because the simple model adopted a crude convective parametrization scheme and involved a number of assumptions. The simulated MJO structure is too symmetric about the equator, with a too strong Kelvin wave component presented. It is desirable to conduct parallel numerical experiments with a full-physics general circulation model. The conclusion derived from the simple model about the relative role of the background vertical shear and moisture changes associated with ENSO is tentative. A further in-depth investigation is needed.

Compared to the distinctive contrast between EP El Niño and La Niña, the MJO pattern evolution over the MC resembled more like the long-term climatology during CP El Niño. It is speculated that the cause of a weaker CP El Niño impact might result from a weaker and westward-shifting circulation response over the western North Pacific during CP El Niño, which was caused by a combined effect of nonlinear moisture enthalpy advection and the zonal shifting of anomalous heating (Chen et al., 2019; Wang et al., 2019). While the current study focused on the ENSO impact on the MJO, it would be interesting to extend the current scope to examine the upscale feedback of the MJO to the ENSO.

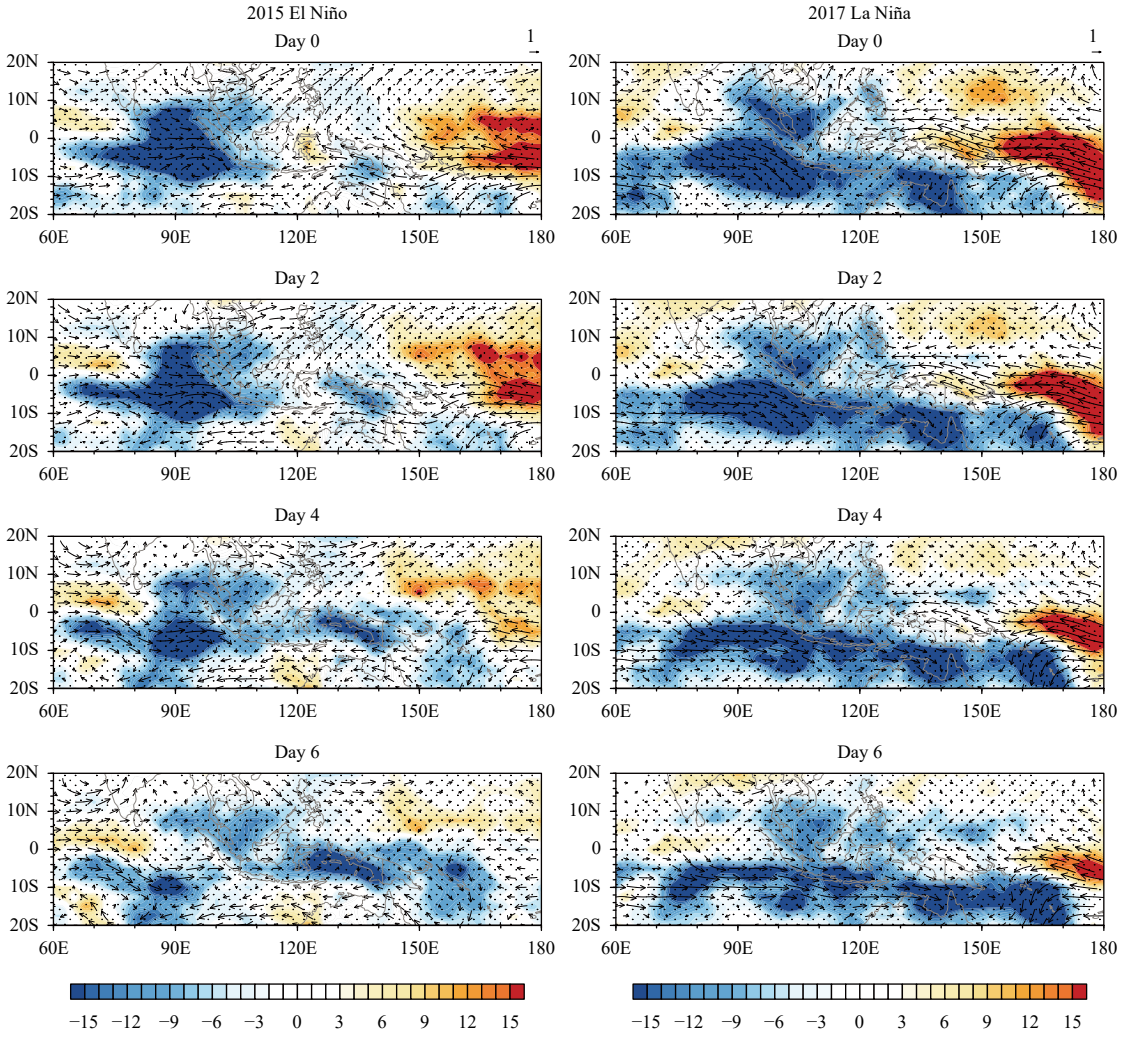

Fig. 15. Lead–lag regressed patterns of 10–90-day filtered OLR anomaly (shaded; W m^{-2}) and associated wind anomaly field at 850 hPa (vector; m s^{-1}) from Days 0 to 6. The regression was based on the OLR anomaly at a reference point over Indian Ocean (5°S, 95°E) during 2015 El Niño (left) and 2017 La Niña (right) winter (DJF), respectively. The OLR anomalies that pass the significant test at 95% confidence level are stippled.

REFERENCES

Ashok, K., H. Nakamura, and T. Yamagata, 2007: Impacts of ENSO and Indian Ocean dipole events on the Southern Hemisphere storm-track activity during austral winter. *J. Climate*, **20**, 3147–3163, doi: 10.1175/JCLI4155.1.

Chen, M. C., T. Li, and X. H. Wang, 2019: Asymmetry of atmospheric responses to two-type El Niño and La Niña over Northwest Pacific. *J. Meteor. Res.*, **33**, 826–836, doi: 10.1007/s13351-019-9022-0.

Chen, X., J. Ling, and C. Y. Li, 2016: Evolution of the Madden–Julian oscillation in two types of El Niño. *J. Climate*, **29**, 1919–1934, doi: 10.1175/JCLI-D-15-0486.1.

Chung, P.-H., and T. Li, 2013: Interdecadal relationship between the mean state and El Niño types. *J. Climate*, **26**, 361–379, doi: 10.1175/JCLI-D-12-00106.1.

Deng, L., and T. Li, 2016: Relative roles of background moisture and vertical shear in regulating interannual variability of boreal summer intraseasonal oscillations. *J. Climate*, **29**, 7009–7025, doi: 10.1175/JCLI-D-15-0498.1.

Deng, L., T. Li, J. Liu, et al., 2016: Factors controlling the interannual variations of MJO intensity. *J. Meteor. Res.*, **30**, 328–340, doi: 10.1007/s13351-016-5113-3.

Ge, X. Y., T. Li, and X. Q. Zhou, 2007: Tropical cyclone energy dispersion under vertical shears. *Geophys. Res. Lett.*, **34**, L23807, doi: 10.1029/2007GL031867.

Gill, A. E., 1980: Some simple solutions for heat-induced tropical circulation. *Quart. J. Roy. Meteor. Soc.*, **106**, 447–462, doi: 10.1002/qj.49710644905.

Hendon, H. H., and M. L. Salby, 1994: The life cycle of the Madden–Julian oscillation. *J. Atmos. Sci.*, **51**, 2225–2237, doi: 10.1175/1520-0469(1994)051<2225:TLCOTM>2.0.CO;2.

Jiang, X. N., T. Li, and B. Wang, 2004: Structures and mechanisms of the northward propagating boreal summer intraseasonal oscillation. *J. Climate*, **17**, 1022–1039, doi: 10.1175/1520-0442(2004)017<1022:SAMOTN>2.0.CO;2.

Jiang, X. N., D. E. Waliser, P. K. Xavier, et al., 2015: Vertical structure and physical processes of the Madden–Julian oscil-

lation: Exploring key model physics in climate simulations. *J. Geophys. Res. Atmos.*, **120**, 4718–4748, doi: 10.1002/2014JD022375.

Kao, H.-Y., and J.-Y. Yu, 2009: Contrasting eastern-Pacific and central-Pacific types of ENSO. *J. Climate*, **22**, 615–632, doi: 10.1175/2008JCLI2309.1.

Krishnamurti, T. N., and D. Subrahmanyam, 1982: The 30–50 day mode at 850 mb during MONEX. *J. Atmos. Sci.*, **39**, 2088–2095, doi: 10.1175/1520-0469(1982)039<2088:TDMAMD>2.0.CO;2.

Li, T., 2006: Origin of the summertime synoptic-scale wave train in the western North Pacific. *J. Atmos. Sci.*, **63**, 1093–1102, doi: 10.1175/JAS3676.1.

Li, T., 2010: Monsoon climate variabilities. *Climate Dynamics*: *Why Does Climate Vary?* Sun, D.-Z., and F. Bryan, Eds., American Geophysical Union, Washington, DC, 27–51, doi: 10.1029/2008GM000782.

Li, T., and B. Wang, 2005: A review on the western North Pacific monsoon: Synoptic-to-interannual variabilities. *Terr. Atmos. Oceanic Sci.*, **16**, 285–314, doi: 10.3319/TAO.2005.16.2.285(A).

Li, T., and C. H. Zhou, 2009: Planetary scale selection of the Madden–Julian oscillation. *J. Atmos. Sci.*, **66**, 2429–2443, doi: 10.1175/2009JAS2968.1.

Li, T., and P.-C. Hsu, 2018: *Fundamentals of Tropical Climate Dynamics*. Springer, Cham, Switzerland, 61–106.

Li, T., B. Wang, C.-P. Chang, et al., 2003: A theory for the Indian Ocean dipole–zonal mode. *J. Atmos. Sci.*, **60**, 2119–2135, doi: 10.1175/1520-0469(2003)060<2119:ATFTIO>2.0.CO;2.

Li, T., B. Wang, B. Wu, et al., 2017: Theories on formation of an anomalous anticyclone in western North Pacific during El Niño: A review. *J. Meteor. Res.*, **31**, 987–1006, doi: 10.1007/s13351-017-7147-6.

Li, T., J. Ling, and P.-C. Hsu, 2020: Madden–Julian oscillation: Its discovery, dynamics, and impact on East Asia. *J. Meteor. Res.*, **34**, 20–42, doi: 10.1007/s13351-020-9153-3.

Li, T. M., and B. Wang, 1994: The influence of sea surface temperature on the tropical intraseasonal oscillation: A numerical study. *Mon. Wea. Rev.*, **122**, 2349–2362, doi: 10.1175/1520-0493(1994)122<2349:TIOSST>2.0.CO;2.

Lin, A. L., and T. Li, 2008: Energy spectrum characteristics of boreal summer intraseasonal oscillations: Climatology and variations during the ENSO developing and decaying phases. *J. Climate*, **21**, 6304–6320, doi: 10.1175/2008JCLI2331.1.

Lu, J. H., T. Li, and L. Wang, 2019: Precipitation diurnal cycle over the Maritime Continent modulated by the MJO. *Climate Dyn.*, **53**, 6489–6501, doi: 10.1007/s00382-019-04941-8.

Madden, R. A., and P. R. Julian, 1971: Detection of a 40–50 day oscillation in the zonal wind in the tropical Pacific. *J. Atmos. Sci.*, **28**, 702–708, doi: 10.1175/1520-0469(1971)028<0702:DOADOI>2.0.CO;2.

Madden, R. A., and P. R. Julian, 1972: Description of global-scale circulation cells in the tropics with a 40–50 day period. *J. Atmos. Sci.*, **29**, 1109–1123, doi: 10.1175/1520-0469(1972)029<1109:DOGSCC>2.0.CO;2.

Maloney, E. D., 2009: The moist static energy budget of a composite tropical intraseasonal oscillation in a climate model. *J. Climate*, **22**, 711–729, doi: 10.1175/2008JCLI2542.1.

Murakami, T., and T. Nakazawa, 1985: Tropical 45 day oscillations during the 1979 Northern Hemisphere summer. *J. Atmos. Sci.*, **42**, 1107–1122, doi: 10.1175/1520-0469(1985)042<1107:TDODTN>2.0.CO;2.

Neelin, J. D., and I. M. Held, 1987: Modeling tropical convergence based on the moist static energy budget. *Mon. Wea. Rev.*, **115**, 3–12, doi: 10.1175/1520-0493(1987)115<0003:MTCBOT>2.0.CO;2.

Ramage, C. S., 1968: Role of a tropical "maritime continent" in the atmospheric circulation. *Mon. Wea. Rev.*, **96**, 365–370, doi: 10.1175/1520-0493(1968)096<0365:ROATMC>2.0.CO;2.

Raymond, D. J., 2000: Thermodynamic control of tropical rainfall. *Quart. J. Roy. Meteor. Soc.*, **126**, 889–898, doi: 10.1002/qj.49712656406.

Raymond, D. J., 2001: A new model of the Madden–Julian oscillation. *J. Atmos. Sci.*, **58**, 2807–2819, doi: 10.1175/1520-0469(2001)058<2807:ANMOTM>2.0.CO;2.

Rong, X. Y., R. H. Zhang, T. Li, et al., 2011: Upscale feedback of high-frequency winds to ENSO. *Quart. J. Roy. Meteor. Soc.*, **137**, 894–907, doi: 10.1002/qj.804.

Sobel, A., and E. Maloney, 2012: An idealized semi-empirical framework for modeling the Madden–Julian oscillation. *J. Atmos. Sci.*, **69**, 1691–1705, doi: 10.1175/JAS-D-11-0118.1.

Sobel, A., and E. Maloney, 2013: Moisture modes and the eastward propagation of the MJO. *J. Atmos. Sci.*, **70**, 187–192, doi: 10.1175/JAS-D-12-0189.1.

Sobel, A. H., J. Nilsson, and L. M. Polvani, 2001: The weak temperature gradient approximation and balanced tropical moisture waves. *J. Atmos. Sci.*, **58**, 3650–3665, doi: 10.1175/1520-0469(2001)058<3650:TWTGAA>2.0.CO;2.

Wang, B., and T. M. Li, 1993: A simple tropical atmosphere model of relevance to short-term climate variations. *J. Atmos. Sci.*, **50**, 260–284, doi: 10.1175/1520-0469(1993)050<0260:ASTAMO>2.0.CO;2.

Wang, B., and T. M. Li, 1994: Convective interaction with boundary-layer dynamics in the development of a tropical intraseasonal system. *J. Atmos. Sci.*, **51**, 1386–1400, doi: 10.1175/1520-0469(1994)051<1386:CIWBLD>2.0.CO;2.

Wang, B., and X. S. Xie, 1996: Low-frequency equatorial waves in vertically sheared zonal flow. Part I: Stable waves. *J. Atmos. Sci.*, **53**, 449–467, doi: 10.1175/1520-0469(1996)053<0449:LFEWIV>2.0.CO;2.

Wang, B., and X. S. Xie, 1997: A model for the boreal summer intraseasonal oscillation. *J. Atmos. Sci.*, **54**, 72–86, doi: 10.1175/1520-0469(1997)054<0072:AMFTBS>2.0.CO;2.

Wang, B., R. G. Wu, and T. Li, 2003: Atmosphere–warm ocean interaction and its impacts on Asian–Australian monsoon variation. *J. Climate*, **16**, 1195–1211, doi: 10.1175/1520-0442(2003)16<1195:AOIAII>2.0.CO;2.

Wang, L., T. Li, E. Maloney, et al., 2017: Fundamental causes of propagating and nonpropagating MJOs in MJOTF/GASS models. *J. Climate*, **30**, 3743–3769, doi: 10.1175/JCLI-D-16-0765.1.

Wang, L., T. Li, L. Chen, et al., 2018: Modulation of the MJO intensity over the equatorial western Pacific by two types of El Niño. *Climate Dyn.*, **51**, 687–700, doi: 10.1007/s00382-017-3949-6.

Wang, X. H., T. Li, and M. C. Chen, 2019: Mechanism for asymmetric atmospheric responses in the western North Pacific to El Niño and La Niña. *Climate Dyn.*, **53**, 3957–3969, doi:

10.1007/s00382-019-04767-4.

Wu, B., T. J. Zhou, and T. Li, 2009: Seasonally evolving dominant interannual variability modes of East Asian climate. *J. Climate*, **22**, 2992–3005, doi: 10.1175/2008JCLI2710.1.

Wu, B., T. Li, and T. J. Zhou, 2010: Asymmetry of atmospheric circulation anomalies over the western North Pacific between El Niño and La Niña. *J. Climate*, **23**, 4807–4822, doi: 10.1175/2010JCLI3222.1.

Xiang, B. Q., B. Wang, and T. Li, 2013: A new paradigm for the predominance of standing central Pacific warming after the late 1990s. *Climate Dyn.*, **41**, 327–340, doi: 10.1007/s00382-012-1427-8.

Yeh, S.-W., J.-S. Kug, B. Dewitte, et al., 2009: El Niño in a changing climate. *Nature*, **461**, 511–514, doi: 10.1038/nature 08316.

Yuan, Y., C. Y. Li, and J. Ling, 2015: Different MJO activities between EP El Niño and CP El Niño. *Sci. Sinica Terr.*, **45**, 318–334, doi: 10.1360/zd-2015-45-3-318. (in Chinese)

Zhang, Y., T. Li, J. Y. Gao, et al., 2020: Origins of quasi-biweekly and intraseasonal oscillations over the South China Sea and Bay of Bengal and scale selection of unstable equatorial and off-equatorial modes. *J. Meteor. Res.*, **34**, 137–149, doi: 10.1007/s13351-020-9109-7.

Zhao, C. B., T. Li, and T. J. Zhou, 2013: Precursor signals and processes associated with MJO initiation over the tropical Indian Ocean. *J. Climate*, **26**, 291–307, doi: 10.1175/JCLI-D-12-00113.1.

Zhu, W. J., T. Li, X. H. Fu, et al., 2010: Influence of the Maritime Continent on the boreal summer intraseasonal oscillation. *J. Meteor. Soc. Japan*, **88**, 395–407, doi: 10.2151/jmsj.2010308.

Tech & Copy Editor: Qi WANG